21st European Conference on Fracture, ECF21, 20-24 June 2016, Catania, Italy

Numerical investigation of dynamic strain ageing and slant ductile fracture in a notched specimen and comparison with synchrotron tomography 3D-DVC

S.-C. Ren[a,*], G. Rousselier[a,*], T.F. Morgeneyer[a,*], M. Mazière[a], S. Forest[a]

[a]MINES ParisTech, PSL Research University, MAT-Centre des matriaux, CNRS UMR 7633, BP 87 91003 Evry, France

Abstract

In ductile tearing experiments, a flat crack is often observed to develop normal to the loading direction that subsequently turns into a slant crack. The underlying physical mechanisms are poorly understood. The numerical strategy for reproducing such kind of slant fracture remains a challenge. Recently, the strain field of a 2198 aluminium alloy CT-like specimen has been measured by lamino(tomo-)graphy combined with digital volume correlation (DVC) (Morgeneyer et al. (2014)). Multiple localisation bands were observed at notch area at early loading stages. The final fracture occurred within an inclined band. Experiments showed evidences of Portevin-Le Chatelier (PLC) effect in this alloy at room temperature. Previous simulations with von Mises, anisotropic plasticity or Gurson-Tvergaard-Needleman (GTN) models were not able to simulate these observations. As the PLC effect produces instabilities and multiple inclined localisation bands, it is considered to be a candidate for the underlying mechanism related to slant fracture. A fully coupled model (Rousselier and Quilici (2015)) combining polycrystalline, PLC, porous plasticity and Coulomb fracture implemented in FE code is used for simulating these phenomena. The PLC model gives intermittent and moving oscillations of the macroscopic plastic strain rate bands. The multiple strain localisation bands obtained by FE simulation for a thin sheet CT-like specimen are similar to the ones observed in laminography with 3D DVC. Crack propagation occurs during strain rate surges. A flat to slant fracture surface observed in laminography is reproduced successfully by the current FE simulation.

1. Introduction

Fracture in thin sheet tearing test is observed to propagate initially on a flat surface and subsequently turned into a plane with an angle at about 45° to the initial flat plane. This phenomenon has been widely observed in the literature (Pardoen et al. (2004)). The simulation of those phenomena remains a challenge due to lack of understanding of the mechanism and numerical difficulties. The early stage localisation might be an important influencing factor. Hickey and Ravi-Chandar (2016) studied damage in SENT specimens of 6061 aluminium alloy at two different states (T6

---

* Corresponding authors.
  E-mail address: sicong.ren@mines-paristech.fr; gilles.rousselier@mines-paristech.fr; thilo.morgeneyer@mines-paristech.fr;
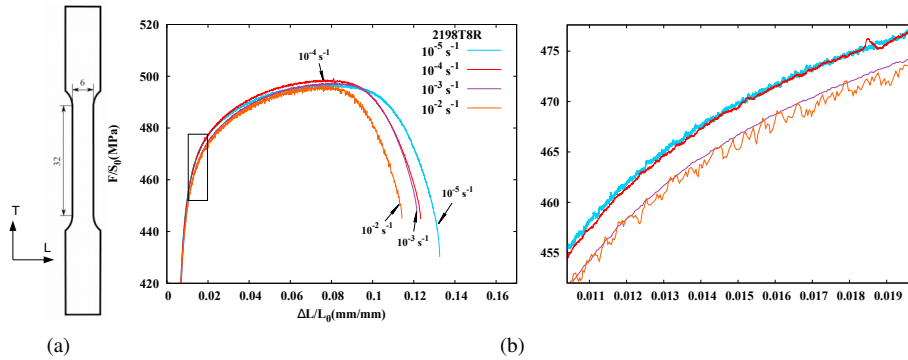
Fig. 1: (a) Specimen geometry; (b) Tensile stress-strain curves of 2198T8R tested at room temperature and the zoom area indicated by a square frame.

and O) with the help of digital image correlation (DIC) measurement. Two kinds of plastic strain localized zones that precedes fracture were observed and recognized as the origin of the two fracture mode: flat (or cup-cone) and slant. Recent observations by in-situ synchrotron X-ray laminography verified the existence of multiple localisation bands at early loading stage ahead of the notch of 2198 alloy CT-like specimen (Morgeneyer et al. (2014)). The final fracture occurred within an inclined localisation band.

The different fracture modes of tensile specimens tested inside and outside PLC sensitive zone have been reported by some authors like Wang et al. (2011), Fu et al. (2011) and Clausen et al. (2004). Slant fractures only occurred within the PLC temperature (or strain rate) range. At other temperatures (or strain rate) without PLC effect, the fracture mode showed typical flat or cup-cone form. Under certain circumstance, spiral (double) shear lip zones were found around the central fibrous zone of cup-cone like fracture surface (Verma et al. (2015)). For tests outside PLC zone, the spiral shear lip zone is vanished and replaced by the usual cup-cone fracture surface. For tearing specimens with larger geometry, the fracture surface even showed unstable flip-flop feature (Simonsen and Törnqvist (2004)). These characteristics made a possible link to the dynamic strain ageing effect (or Portevin-Le Chatelier, PLC), which is activated within certain strain rate and temperature range and produces slanted unstable localisation bands.

In this paper, tensile test performed to investigate the possible PLC effect in 2198T8R are presented. The finite element simulations of a CT specimen with a constitutive model coupling polycrystalline plasticity, PLC, porous plasticity and Coulomb fracture aiming at reproducing laminography observations especially the slant fracture were exhibited.

2. Experimental observations

2.1. Material

AA2198 alloy is a new generation of low density Al-Cu-Li alloy developed in the current decade, which is starting to be applied for the fuselage and some components of wings of the latest aircraft like A350 and the rocket Falcon 9 of SpaceX. Copper ($\sim$ 3.41 wt%) and Lithium ($\sim$ 0.94 wt%) are the primary alloying elements in this material. Lithium (Li) is added to increase the strength and to reduce density of the alloy, which also participates in the formation of $T1$, T_2 and θ'-type precipitates. Comparing to the two previous generations of Al-Cu-Li alloys, AA2198 has lower lithium and higher copper content.

The received 2.0 mm thick material sheet, provided by Constellium, is in the recrystallized state and after an artificial ageing treatment (T8). The initial porosity was very low (< 0.03 vol%). No additional treatment was applied before testing. The rolling direction of material processing is marked by (L), transverse direction by (T) and the short-transverse direction in the through thickness by (S). The grain size was measured by Chen (2011) using a mean linear intercept method: 200-300 μm along rolling direction (L), 60 μm in long transverse direction (T) and 25-30 μm in short transverse direction (S).
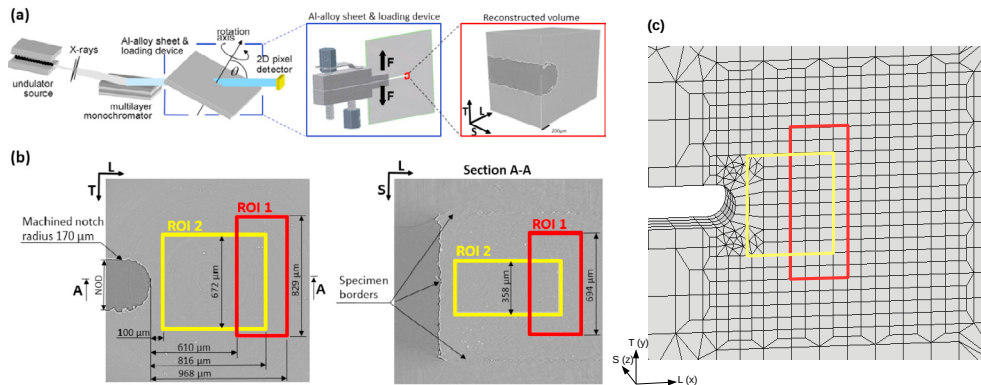
Fig. 2: (a) Schematic review of the laminography experimental set-up (reproduced from Buljac et al. (2015)) . (b) ROI position in the reconstructed volume sections. ROI 1 corresponds to the ROI volume studied by Morgeneyer et al. (2014) (c) corresponding ROI positions in FE mesh (view from the middle plane z = 0 mm).

2.2. Tensile tests

The specimens were prepared in the T-L plane of material sheet with loading axis along T direction. The specimen presents an initial gage length L_0 = 25 mm and thickness of 2.0 mm (see Fig. 1(a)). Tests were conducted on a MTS10t servo-hydraulic tensile machine. The load cell measuring range is 0~100 kN. Tensile tests were carried out at room temperature under displacement control with different strain rates from $10^{-2}s^{-1}$ to $10^{-4}s^{-1}$. The stress-strain curves are plotted in Fig. 1(b). A weak negative strain rate sensitivity and some serrated plastic flow can be observed which suggest the existence of PLC effect in this material. Tensile tests were also performed on the 2198T3R, which has the same chemical composition and similar texture but a different heat treatment with 2198T8R. The PLC effect is more significant for the T3 state material. Using digital image correlation, a clear propagating strain rate localisation band (type A) could be seen on the spatio-temporal pattern figure for T3 state specimen tested at $10^{-2}s^{-1}$ and $10^{-3}s^{-1}$. For 2198T8R, only blur heterogeneous strain rate fields could be observed, though their magnitude were definitely higher than measurement noises. Those heterogeneities could be related to the type C serrations that correspond to randomly nucleated non-propagating bands appeared with a small amplitude and high frequency. As the PLC effect is sensitive to temperature and strain rate, the current test conditions seem to be located around the lower boundary of the PLC sensitive zone (see Fig. 3 in Lebyodkin et al. (2000)). Further tests will be performed in a lower temperature.

2.3. Laminography and DVC

A CT-like specimen (with dimension: width W = 60 mm, height H = 70 mm, thickness B = 1 mm, notch length a = 36 mm, notch radius r = 0.17 mm) was investigated by the in situ X-ray laminography at the European Synchrotron Radiation Facility (ESRF, Grenoble, France) by Morgeneyer et al. (2014) and Buljac et al. (2015). A schematic review of the laminography experimental set-up is shown in Fig. 2(a). A 3-D reconstructed volume of the notch area in the initial unloaded state is also shown in Fig. 2(a). Two regions of interests (ROIs) were taken into consideration. Their positions are presented in Fig. 2(b). The corresponding positions in the FE mesh are marked in Fig. 2(c). The strain fields after each loading step in ROI 1 have been analysed by Morgeneyer et al. (2014). Recently, Buljac et al. (2015) reported the results about ROI 2. Both of theses results will be discussed in the FE simulation part.

A stepwise loading was applied in the T-L plane perpendicular to the notch plane through a two-screws loading device. After each loading, the notch opening displacement (NOD), measured at a point ~200 μm behind the original notch tip, was maintained. The region ahead of the notch was scanned by laminography in the initial unloaded state and after each load step. The NOD steps are given in table 1. The laminography-DVC results will be shown together with FE simulation results in section 4.

Table 1: Loading steps of laminography scan and corresponding notch opening displacement (NOD) (Morgeneyer et al. (2014)).

Load step	0	1	2	3	4
NOD (μm)	0	56	101	127	177

3. Constitutive equations coupled with PLC model

3.1. Polycrystalline model

The current model is build in the polycrystalline framework. For reducing computational cost, the reduced texture methodology (RTM) (Rousselier et al. (2009, 2010, 2012)) is used. The viscoplastic constitutive equations for each slip system takes the following form (Cailletaud (1996)):

$$
\begin{aligned}
&\dot{\gamma}_s = \dot{v}_s \text{Sign}(\tau_s - X_s), \\
&\dot{v}_s = \left\langle \left(\frac{|\tau_s - X_s| - r_s}{K} \right)^n \right\rangle, \quad \text{where} \quad \langle f \rangle = \text{Max}(0, f) \\
&r_s = r_s(v_s, v_t), \quad \forall t \neq s, \\
&\dot{\alpha}_s = \dot{\gamma}_s - d\alpha_s \dot{v}_s, \quad X_s = c\alpha_s.
\end{aligned}
\tag{1}
$$

where $\dot{\gamma}_s$ and τ_s are respectively the slip rate and resolved shear stress of each slip system. The index s is the number of slip system ($s = 1$ to M); In the case of FCC crystallographic structures, $M = 12$. r_s denotes the isotropic hardening; X_s represents the kinematic part. To distinguish between different contributions to the hardening term, the classical isotropic hardening law for each slip system is noted by $r_s^{crystal}$

$$
r_s^{crystal} = R_s + Q_1 \sum_{t=1}^{M} H_{st} \left[1 - \exp(-b_1 \gamma_t) \right] + Q_2 \sum_{t=1}^{M} K_{st} \left[1 - \exp(-b_2 \gamma_t) \right],
\tag{2}
$$

where R_s is the initial critical resolved shear stress (CRSS), which is assumed to be identical for all octahedral slip systems. The diagonal terms of matrix $H_{st}(s = t)$ represent the self-hardening of each system, and the non-diagonal terms ($s \neq t$) represent the latent hardening. The third term on the right side of equation 2 is devoted to characterising the evolution of the hardening matrix at large strains. The hardening matrix K_{st} takes the form as same as H_{st}, which is a 12×12 symmetric matrix depending on six parameters (h_1 to h_6, see Rousselier et al. (2009) for more details).

3.2. PLC model

The KEMC type strain ageing model (Kubin and Estrin (1985); McCormick and Ling (1995); Graff et al. (2004); Mazière et al. (2010); Wang et al. (2012)) is based on an elastoviscoplastic phenomenological aspect. It has been widely used in the literature for simulating strain ageing effect. In this kind of model, the ageing time t_a, which denotes the effective time that the arrested mobile dislocations have aged, is introduced as an internal variable. The change of ageing time induces a variation of the relative concentration of solute atoms pinning the mobile dislocations that can further cause instabilities on the stress strain curve and localisation caused by local softening due to stress drop. The KEMC model allows the prediction of both static strain ageing (SSA; Lüders effect) and dynamic strain ageing (DSA; PLC effect). In the current work, the KEMC model is formulated at the slip system scale. The dynamic strain ageing at each slip system is considered to be an individual action. The DSA term takes the following form

$$
\begin{aligned}
&r_s^{DSA} = P_1 \phi, \qquad \phi = \left[1 - \exp\left(-P_2 (\gamma_s)^\alpha t_a^\beta \right) \right], \\
&\dot{t}_a = 1 - \frac{\dot{\gamma}_s}{\omega} t_a, \quad t_a(t = 0) = t_{a0}
\end{aligned}
\tag{3}
$$

where ϕ is the relative concentration of solute atoms pinning the mobile dislocations ($\phi \in [0, 1]$). P_1 is the maximal stress drop magnitude from pined state $\phi = 1$ to unpinned state $\phi = 0$. P_2, α and n are constants. ω is the strain

increment produced during a pinning-relaxation process. t_{a0} is the initial ageing time which is related to the simulation of SSA effect. Then the DSA hardening term r_s^{DSA} together with the classical hardening term $r_s^{crystal}$ constitute the total isotropic hardening in a slip system r_s.

$$r_s = r_s^{crystal} + r_s^{DSA} \tag{4}$$

3.3. Coulomb fracture

Considering shear fracture occurs by shear localisation at the grain scale without void damage, the Coulomb fracture model is also formulated at the slip system scale. Prior to shear localisation and fracture, a large amount of plastic deformation is demanded. To describe this phenomenon, an additional slip rate $\dot{\gamma}_s^C$ activated at large strain is added to the slip rate $\dot{\gamma}_s$ in eq. (1)

$$\dot{\gamma}_s^C = \left\langle \left(\frac{|\tau_s| + c_0 \sigma_{ns} - R_0 \exp(-b_0 \gamma_s^C)}{K} \right)^n \right\rangle \mathrm{Sign}(\tau_s) \tag{5}$$

where σ_{ns} is the stress normal to the slip plane. c_0 and R_0 are parameters to be calibrated. b_0 is a constant.

3.4. Damage model

The Rousselier damage model is reformulated in the polycrystalline framework (Rousselier and Quilici (2015)). The yield function reads

$$F = \frac{\sigma_{eq}}{1-f} - \left(\sum_{g=1}^{N} f_g \sigma_g \right)_{eq} + D_1 f \sigma_1 \exp\left(\frac{\sigma_m}{(1-f)\sigma_1} \right) \tag{6}$$

where f is the void volume fraction. D_1 and σ_1 are material parameters. The second term on the right side of eq. (6) is the polycrystalline matrix equivalent stress. Each of the N represents a "phase" in a polycrystalline matter, which is made of a set of physical grains with close orientations. f_g is the volume fraction of phase g referring to the matrix, i.e. $(1-f)f_g$ referring to the total volume. The stress σ_g and ε_g are assumed to be be homogeneous in each phase (see e.g. Rousselier and Luo (2014) for detailed equation). The macroscopic stress and strain are then defined as the superposition of the spatial average of σ_g and ε_g over N phases. The stresses at the macroscopic and microscopic (i.e. crystal) scale are related by the "β-rule" (see Cailletaud (1996); Rousselier and Luo (2014)).

To sum up, the macroscopic plastic strain rate is:

$$\dot{\underline{\varepsilon}}^p = (1-f) \sum_{g=1}^{N} f_g \sum_{s=1}^{M} \underline{m}_{sg} (\dot{\gamma}_s + \dot{\gamma}_s^C) + \frac{f}{3} D_1 \exp\left(\frac{\sigma_m}{(1-f)\sigma_1} \right) \dot{\varepsilon}_{eq}^p \underline{1} \tag{7}$$

where $\underline{m}_{sg}$ is the orientation matrix of each slip system; $\underline{1}$ is the unity matrix; $\dot{\varepsilon}_{eq}^p$ is calculated by taking the second invariant of the deviatoric part. The last term of eq. (7) is the volumetric strain rate, derived from eq. (6). PLC and Coulomb model are included in the first term on the right side of eq. (7).

4. FEM simulations

The mesh in the notch region is presented in Fig. 2(c). Identical elements are used in this region whose dimension is (x = 0.125) × (y = 0.10) × (z = 0.125) mm^3. The notch tip is at x = 36 mm. The 1 mm thickness is divided into 8 elements. The loading time for each step in the experiments was not precisely controlled but rather stable (Buljac et al. (2015); Morgeneyer et al. (2014)), here we made a hypothesis that the duration for each loading was constant and equal to 1 minute, which is certainly a lower limit of the applied strain rates. Thus, displacements at a constant velocity of 10^{-3} mm/s were applied as loading conditions through two "rigid" triangular blocks (see e.g. Fig. 12(a) in Morgeneyer et al. (2014)). The positions of these two blocks are determined according to experimental conditions. To prevent body motion, the point at (x = 60 mm, y= 0 mm, z= 0 mm) is fixed. To prevent buckling, the displacement U_z is set to be 0 at the mid-plane z = 0 mm of the area surrounding the critical notch zone.
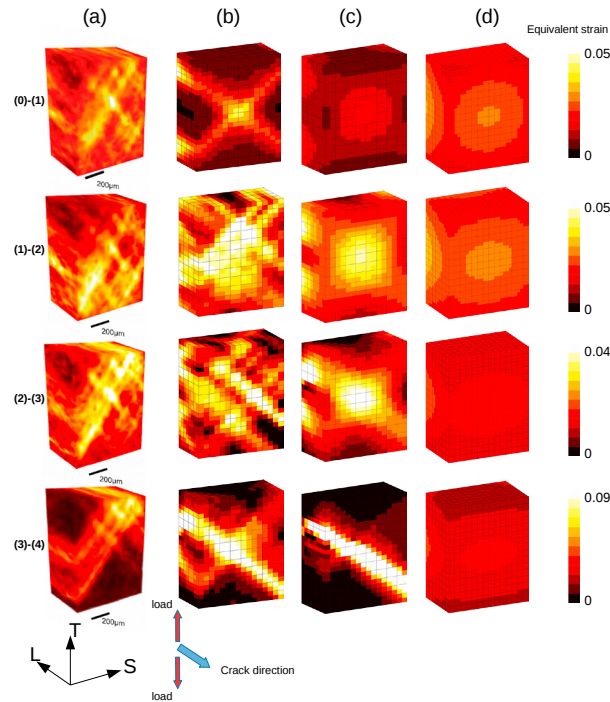
Fig. 3: von Mises equivalent strain field in ROI 1 of increments (0)-(1), (1)-(2), (2)-(3) and (3)-(4). (a) Laminography-DVC analysis (Morgeneyer et al. (2014)); (b) Current full coupled model; (c) without PLC effect (polycrystalline+damage+Coulomb) (d) Tresca plasticity

.

4.1. Equivalent strain fields

Fig. 3 shows the incremental equivalent strain fields in the ROI 1 for four increments: step (0)-(1), step (1)-(2), step (2)-(3), step (3)-(4). These incremental equivalent strain fields were measured by the correlations between the current step and the previous one, i.e. the results of (1)-(2) is obtained by comparing the strain magnitude at step 2 with that at step 1. This strategy makes the localisation bands easier to be observed than the cumulated ones, that are always compared with the initial unloaded state. Fig. 3(a) is the laminography-DVC measurement of the equivalent strain fields reported by Morgeneyer et al. (2014). Multiple localisation bands were observed in front of the notch tip (∼ 970 μm) at very early stage of loading steps.

Fig. 3(b) presents the simulation results in the ROI 1 with the current full coupled model. At step (0)-(1), two orthogonal strain localisation bands are observed, which produced a highlighted area at band intersection. However, these two bands showed similar strain magnitude. In the experimental observation, a main slant band from the upper-right corner to the lower-left corner is more activated than the other (see Fig. 3(a)). The material heterogeneity and real loading conditions in the experiment can obviously favour the appearance of a non-symmetric strain field. At step (1)-(2) and (2)-(3), the band activities became more active which are the same as the laminography observations. At step (1)-(2), a lot of smaller bands perpendicular or parallel to the two orthogonal bands are distributed over a large area in the ROI. At step (2)-(3), the bands began to lighten only in the area surrounding one of the two orthogonal bands (from upper-left to lower-right). Finally, a narrowing slanted localisation band was formed in this zone. The orientation of bands is approximately 45° to the loading direction both in the FE simulation and in experiments. The evolution of strain localisation band pattern is qualitatively in agreement with laminography observations, though the pattern is not strictly identical. We can not expect a completely deterministic prediction with PLC model who involves intrinsic instabilities.

To compare with the situation without PLC effect, the PLC term is eliminated by setting $P_1 = 0$ MPa and $R_s = 181$ MPa in lieu of $P_1 = 80$ MPa and $R_s = 101$ MPa. Fig. 3(c) gives the equivalent strain field obtained by eliminating the
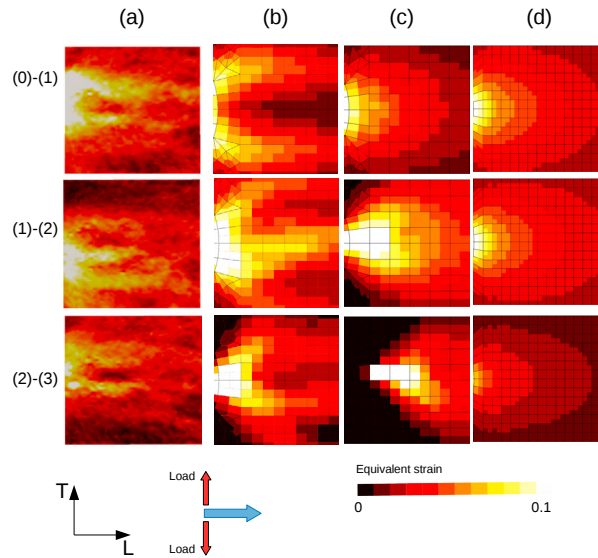
Fig. 4: Incremental von Mises equivalent strain field in the T-L plane of ROI 2. (a) Laminography-DVC analysis at z = 0 mm (Buljac et al. (2015)); (b) Current full coupled model (z = -0.25 mm); (c) without PLC term at z = -0.125 mm (polycrystalline+damage+Coulomb); (d) Tresca (approximated using Bron) plasticity (z = 0 mm).

PLC term, i.e. Rousselier damage model and Coulomb fracture criterion together in the polycrystalline framework. The multiple bands could not be observed any more. Strain began to concentrate along one slanted area at increment (2)-(3) and finally a slanted localisation band suddenly appeared at increment (3)-(4). As the stress level in this new trial without PLC is higher than that with PLC, the influence of Coulomb criterion is enhanced which advanced the crack propagation (initiated at increment (2)-(3)). Fig. 3(d) shows the simulation with Tresca plasticity. It is clear that it is not enough to reproduce the experimental observations especially the slant fracture. Other simulations using GTN model and von Mises plasticity have been reported by Morgeneyer et al. (2014). They did not reproduce the strain localisation bands nor the slant fracture. In Morgeneyer and Besson (2011), transition from flat to slant has been successfully reproduced numerically for a tear test of an aluminium sheet using void nucleation based on the Lode parameter for shear. This model is not supposed to reproduce the initial slant strain concentration band either.

The incremental equivalent strain fields in ROI 2 are shown in Fig. 4(a). More than two bands were observed. At increment (2)-(3), a central band is activated. From increment (1)-(2) to (3)-(4), these bands are activated alternately. These activities are more evident on the specimen surfaces which will not be shown here due to space limitation. Those multiple bands and the alternating activity are not expected from Tresca plasticity (Fig. 4(c)), von Mises plasticity or GTN model. The simulations results using von Mises plasticity and GTN are not presented here.

5. Conclusion and discussion

The strain rate dependent behaviour of the new generation Al-Cu-Li alloy 2198 has been investigated through tensile tests. Experimental observations reveal a negative strain rate sensitivity and unstable plastic flow in 2198T8R aluminium alloy at room temperature. These characteristics are closely related to PLC effect. Propagating strain rate bands have not been observed through DIC measurement for 2198T8R, while a significant evidence of PLC effect is found in its homologue 2198T3R, which will be addressed in a following work.

Finite element simulations were performed on a thin sheet CT-like specimen with different constitutive models, including GTN porous plasticity, Tresca plasticity, von Mises plasticity and a polycrystalline model involving PLC effect proposed by Rousselier and Quilici (2015). The incremental strain fields in ROI 1 and ROI 2 were compared with the DVC results at the same area by each increment characterised by NOD. The multiple localisation bands observed by laminography have been reproduced successfully by the full coupled constitutive model involving PLC

effect. Damage evolves following the early localisation band which is in agreement with experimental observations (Morgeneyer et al. (2014)). The final slant fracture was found to develop within it. Slant fracture has been captured in both simulations with and without PLC term using the polycrystalline based model. However, in the simulation without PLC term, the incremental strain fields are distinct from early PLC-related ones, the latter are more similar to experimental observations. It is reasonable to conclude that PLC effect is responsible for the early state localisations.

Acknowledgements

References

Buljac, A., Taillandier-Thomas, T., Morgeneyer, T. F., Helfen, L., Roux, S., Hild, F., 2015. Slant strained band development during flat to slant crack transition in AA 2198 T8 sheet: in situ 3D measurements. International Journal of Fracture 1–14.

Cailletaud G., 1992. A micromechanical approach to inelastic behaviour of metals. International Journal of Plasticity 8(1), 55–73.

Chen, J. Ductile tearing of AA2198 aluminium-lithium sheets for aeronautic application. Doctoral dissertation. École Nationale Supérieure des Mines de Paris, 2011.

Clausen, A. H., Brvik, T., Hopperstad, O. S., Benallal, A. (2004). Flow and fracture characteristics of aluminium alloy AA5083H116 as function of strain rate, temperature and triaxiality. Materials Science and Engineering: A 364(1), 260–272.

Fu, S., Zhang, Q., Hu, Q., Gong, M., Cao, P., Liu, H., 2011. The influence of temperature on the PLC effect in al-mg alloy. Science China Technological Sciences 54(6), 1389–1393.

Graff, S., Forest, S., Strudel, J. L., Prioul, C., Pilvin, P., Bchade, J. L., 2004. Strain localisation phenomena associated with static and dynamic strain ageing in notched specimens: experiments and finite element simulations. Materials Science and Engineering: A 387, 181–185.

Hickey, W. F., Ravi-Chandar, K., 2016. Transition from Flat to Slant Fracture in Ductile Materials. In Recent Trends in Fracture and Damage Mechanics (pp. 215-235). Springer International Publishing.

Kubin, L. P., Estrin, Y., 1985. The Portevin-Le Chatelier effect in deformation with constant stress rate. Acta Metallurgica 33(3), 397–407.

Lebyodkin, M., Dunin-Barkowskii, L., Brechet, Y., Estrin, Y., Kubin, L. P., 2000. Spatio-temporal dynamics of the PortevinLe Chatelier effect: experiment and modelling. Acta Materialia 48(10), 2529–2541.

Luo M, Rousselier G., 2014. Modeling of large strain multi-axial deformation of anisotropic metal sheets with strength-differential effect using a Reduced Texture Methodology. International Journal of Plasticity 53, 66–89.

Mazière, M., Besson, J., Forest, S., Tanguy, B., Chalons, H., Vogel, F., 2010. Numerical aspects in the finite element simulation of the PortevinLe Chatelier effect. Computer Methods in Applied Mechanics and Engineering 199(9), 734–754.

McCormick, P. G., Ling, C. P., 1995. Numerical modelling of the PortevinLe Chatelier effect. Acta metallurgica et materialia 43(5), 1969–1977.

Morgeneyer, T. F., Taillandier-Thomas, T., Helfen, L., Baumbach, T., Sinclair, I., Roux, S., Hild, F., 2014. In situ 3-D observation of early strain localisation during failure of thin Al alloy (2198) sheet. Acta Materialia 69, 78–91.

Morgeneyer, T. F., Besson, J., 2011. Flat to slant ductile fracture transition: Tomography examination and simulations using shear-controlled void nucleation. Scripta Materialia 65(11), 1002–1005.

Pardoen, T., Hachez, F., Marchioni, B., Blyth, P. H., Atkins, A. G., 2004. Mode I fracture of sheet metal. Journal of the Mechanics and Physics of Solids 52(2), 423–452.

Rousselier, G., Leclercq, S., 2006. A simplified polycrystalline model for viscoplastic and damage finite element analyses. International journal of plasticity 22(4), 685–712.

Rousselier G, Barlat F, Yoon J W., 2009. A novel approach for anisotropic hardening modeling. Part I: Theory and its application to finite element analysis of deep drawing. International Journal of Plasticity 25(12), 2383–2409.

Rousselier G, Barlat F, Yoon J W., 2010. A novel approach for anisotropic hardening modeling. Part II: Anisotropic hardening in proportional and non-proportional loadings, application to initially isotropic material. International Journal of Plasticity 26(7), 1029–1049.

Rousselier G, Luo M, Mohr D., 2012. Macroscopic plasticity modeling of anisotropic aluminum extrusions using a Reduced Texture Methodology. International Journal of Plasticity 30, 144–165.

Rousselier, G., Luo, M., 2014. A fully coupled void damage and MohrCoulomb based ductile fracture model in the framework of a Reduced Texture Methodology. International Journal of Plasticity 55, 1–24.

Rousselier, G., Quilici, S., 2015. Combining porous plasticity with Coulomb and Portevin-Le Chatelier models for ductile fracture analyses. International Journal of Plasticity 69, 118–133.

Simonsen, B. C., Törnqvist, R., 2004. Experimental and numerical modelling of ductile crack propagation in large-scale shell structures. Marine Structures 17(1), 1–27.

Verma, P., Rao, G. S., Chellapandi, P., Mahobia, G. S., Chattopadhyay, K., Srinivas, N. S., Singh, V. (2015). Dynamic strain ageing, deformation, and fracture behavior of modified 9Cr1Mo steel. Materials Science and Engineering: A 621, 39–51.

Wang, H., Berdin, C., Mazire, M., Forest, S., Prioul, C., Parrot, A., Le-Delliou, P., 2011. PortevinLe Chatelier (PLC) instabilities and slant fracture in C-Mn steel round tensile specimens. Scripta Materialia 64(5), 430–433.

Wang, H. D., Berdin, C., Mazière, M., Forest, S., Prioul, C., Parrot, A., Le-Delliou, P., 2012. Experimental and numerical study of dynamic strain ageing and its relation to ductile fracture of a C-Mn steel. Materials Science and Engineering: A 547, 19–31.